> REPLACE THIS LINE WITH YOUR PAPER IDENTIFICATION NUMBER (DOUBLE-CLICK HERE TO EDIT) <   1

Clutter Suppression for Wideband Radar STAP

Di Wu, Daiyin Zhu, *Member, IEEE*, Mingwei Shen, Ning Li, and Huiyu Zhou

Abstract—Space-time adaptive processing (STAP) has been known as a leading technique for airborne/spaceborne radar to detect ground slow-moving targets such as vehicles or tanks. Traditional STAP theory is based on the assumption of narrowband or "zero-bandwidth", where the decorrelation within the space-time snapshot is ignored. However, with radar bandwidths increasing, this assumption becomes invalid, due to the deteriorated decorrelation of the received signals within the space-time snapshot. The decorrelation directly causes the dispersion of the received signals in both spatial and temporal domains, leading to the spreading of the clutter spectrum in the two-dimensional (2D) frequency (Doppler-spatial frequency) domain. With the spreading of the clutter spectrum, the clutter suppression notch in the traditional STAP methods is widened, resulting in a relative poor ability to detect slow-moving targets. In this paper, we focus on the clutter suppression for wideband radar STAP. A general signal model of the ground clutter is first established for the wideband array radar. Using this outcome, we analyze the influence of bandwidth on the 2D spectrum of the ground clutter and quantitatively describe the 2D spreading of the ground clutter on the Doppler-spatial frequency plane. Finally, a 2D keystone transform algorithm, referred to as space-time keystone transform (ST-KT), is proposed to eliminate the spreading of the ground clutter in the 2D frequency domain caused by increasing bandwidths. Simulation results demonstrate that the ST-KT improves the performance of wideband STAP (W-STAP) methods in terms of the output signal-to-clutter plus noise ratio (SCNR) of moving targets.

Index Terms—space-time adaptive processing (STAP); wideband radar; Keystone transform (KT); ground moving target indication (GMTI)

I. INTRODUCTION

Space-time adaptive processing (STAP) is known as a two-dimensional (2D) adaptive filtering technique for airborne surveillance radar to detect ground moving targets within severe and dynamic clutter and jamming environments [1-2]. It is generally recognized that STAP can be seen as an extension of the one-dimensional (1D) spatial-only adaptive array processing, and was first introduced by Brennan and Reed to the radar community in 1973 [3]. Since then, STAP has been vigorously researched, with a number of theories and methods being proposed [4-6].

The early research work of STAP focused mainly on two challenges. The first one is known as computational complexity required by an optimum filter, which approximately reaches the order of $O\{M^3N^3\}$ [2, 4-6], where M denotes the degree of freedom in the temporal domain (the number of the pulses in a coherent processing interval) and N stands for the degree of freedom in the spatial domain (the number of the array elements), primarily due to the covariance matrix's inversion operation. The second is known as slow convergence associated with fully STAP [6-7]. Usually, it is suggested that at least 2MN independent and identically distributed (i.i.d) training samples be required to achieve an average output signal-to-interference plus noise ratio (SINR) loss of 3dB between the fully adaptive and optimal filters [7]. However, this cannot be achieved in a dynamic interference environment. Slow convergence rate coupled with heavy computational burden significantly limits the fully STAP architecture in practical implementations. To address these problems, a diverse set of reduced-dimension STAP [4-6, 8-9] and reduced-rank STAP approaches have been proposed [6, 10-12]. These approaches, adopting sub-optimal adaptive filters instead of the optimal adaptive filter, significantly reduce the computational burden as well as sample requirements, making STAP feasible in practice.

At the end of the last century, by analyzing some measured datasets, such as the mountaintop dataset collected by Defense Advanced Research Projects Agency (DARPA) [13] and the multi-channel airborne radar measurement (MCARM) data collected by the Air Force Research Laboratory at Rome [14], researchers began to pay attention to another challenging problem, i.e., heterogeneous clutter environments, that limits the practical use of STAP [15]. Before this practice, it is usually assumed that the training samples employed to generate 2D weights are i.i.d with the cell under test (CUT). Such training samples are characterized as being homogeneous. However, unfortunately, such sample set is hard to acquire in practice, due to rapidly changing clutter environments. Moreover, a variety of outliers may also be contained in the sample set, making the

situation even worse. Such training samples are characterized as being heterogeneous [15], which causes significant degradation of the established STAP methods. To remedy this, a number of STAP algorithms have been proposed to deal with heterogeneous clutter environments and to reduce the deleterious effects of outliers [15-18]. At the beginning of this century, the knowledge-aided sensor signal processing and expert reasoning (KASSPER) program was developed by DARPA, which promotes the development of a new research branch of STAP, i.e., knowledge-aided STAP (KA-STAP) [19]. This method incorporates a variety of prior knowledge into the traditional training schemes, resulting in promising performance improvement in real-world clutter environments [20-23].

To date, STAP is recognized as an advanced ground moving target detection technique for airborne radar. However, most of the existing STAP approaches suffer from significant performance loss when the instantaneous bandwidth of radar is relatively large. As we have known, traditional STAP methods are based on the assumption of narrowband or "zero-bandwidth", where no decorrelation exists between the signals received on different array elements and at different pulses [2-6]. Nevertheless, when the radar bandwidth increases, the decorrelation of the received signals in either the temporal or the spatial domain can no longer be neglected.

In fact, the influence of bandwidths on adaptive processing was first recognized and investigated in array signal processing [24-25]. The broadened bandwidth causes serious dispersion of interferences across array, leading to deleterious effects on interference-cancellation performance. To handle this problem, a number of wideband (broad band) beamforming and interference cancellation methods were proposed [24-29]. In general, the existing wideband beamforming methods can be categorized into three classes [26], i.e., sub-band processing methods [27], tapped delay line techniques [24, 28], and frequency invariant beamforming methods based on 2D or three-dimensional (3D) arrays [25, 29].

As we know, STAP is originally seen as an extension of the 1D adaptive array signal processing. Hence, with increasing bandwidth, the performance loss for the traditional STAP methods is inevitable [30]. The situation is even worse than that for 1D array processing, as the major undesired signal for STAP, i.e., the echoes of the ground clutter, is correlated both in spatial and temporal domains [31]. Thus, in case of wideband, the decorrelation within the space-time snapshot makes the echo from each ground clutter source disperse across array elements and between pulses. As a result, the 2D spectrum in the Doppler-spatial frequency domain of the ground clutter spreads evidently in both Doppler and spatial frequencies, and thereby degrades the slow-moving target detection performance of the current STAP methods. Moreover, increasing bandwidth also induces increasing mismatches between the actual target steering vector and the ideal steering vector used to calculate the adaptive weight in the traditional STAP architecture, resulting in additional performance loss for the moving targets with different velocities.

It is no doubt that a wideband radar system provides more advantages, such as fine range resolution that benefits the identification and classification of targets. With the development of hardware, an increasing number of new radar systems adopt wideband waveforms instead of narrowband waveforms [1]. Thus, the performance of the so-called wideband STAP (W-STAP) techniques becomes a key factor that affects the moving target detection ability of current and next-generation airborne radar systems.

Generally speaking, current W-STAP approaches can be classified into two classes, i.e., sub-band STAP [32-34] and 3D-STAP [35-37]. The sub-band methods decompose the received data into a parallel bank of sub-bands with the bandwidths narrow enough so that the narrowband assumption is valid. Afterwards, a traditional STAP filter is applied on each of the sub-band data to suppress the interference and the outputs from all the sub-bands are recombined to reconstruct the high-resolution data. It is no doubt that the motivation of using the sub-band methods, i.e., reducing the bandwidth of data that is to be adaptively processed to meet the narrowband assumption, is correct and the improved performance is also verified by simulations. However, it still has obvious drawbacks that greatly limits its practical applications. First, for a bank of say K sub-bands, a single STAP processing thread is repeated K times, which increases the complexity of the system as well as the computational burden. Second, since each channel of the sub-band data undergoes adaptive processing independently, inaccuracy would be introduced more or less when reconstructing the final wideband data, leading to the distortion of waveforms for the moving targets. Finally, the sub-band processing is somewhat like a compromise solution to the problem of wideband clutter, which cannot deal with the clutter spreading thoroughly.

The second type of W-STAP is 3D-STAP, where "3D" refers to spatial, slow-time and fast-time (or equivalently range frequency) domains. In this method, the dimensionality of the adaptive processing problem is increased from NM to NML, where L is the number of the fast-time degree of freedom. The order of the computational complexity increases from $\mathrm{O}\{M^3N^3\}$ to $\mathrm{O}\{M^3N^3L^3\}$, and the demand of i.i.d sample support is increased L times, which are hardly to achieve in practice.

In this paper, we focus our research on clutter suppression for W-STAP. We first establish a general echo signal model of the single ground clutter sources for wideband airborne array radar. Afterwards, the influence of bandwidth on the space-time characteristics of the ground clutter is investigated in detail, and the analytical expressions are derived to quantitatively describe the 2D spreading of each ground clutter source. Then, a 2D space-time keystone transform (ST-KT) algorithm is proposed to eliminate the 2D spreading of the ground clutter, and thereby to improve the performance of W-STAP. As verified by the simulation results later, the proposed 2D ST-KT algorithm can thoroughly cope with the spreading of clutter caused by the increasing bandwidth. Moreover, it also gains the ability to re-focus the moving targets, resulting in the further improvement in terms of the output signal-to-clutter plus noise ratio (SCNR).

This paper was partially presented in [38] while further investigation and extensions are given as follows. First of all, the 2D spreading of ground clutter induced by the increasing bandwidth is analyzed in both the fast-time and fast-time frequency domains, with closed-form expressions to quantitatively describe the direction and extension of the spreading presented. Based on that, the expression of the clutter covariance matrix for W-STAP is provided. We expect that these theoretical works might have reference value for the future research of W-STAP. Besides, the twofold advantage brought by the 2D KT, i.e., the ability to eliminate the 2D clutter spreading and enhance the output power of moving targets meanwhile, is revealed and verified via simulations. Moreover, the proposed ST-KT algorithm is tested not only in the clutter environment but also in the clutter plus jamming environment. The results indicate that the proposed ST-KT algorithm is a promising way for wideband radar to suppress ground clutter and jammings simultaneously.

The rest of this paper is organized as follows. In Section II, a general space-time signal model of single ground clutter sources is established for wideband airborne array radar. In Section III, the influence of bandwidth onto the space-time characteristics of single clutter sources is discussed both in fast-time and fast-time frequency domains. In Section IV, the contributions of the echoes from the ground clutter to a space-time snapshot are discussed when wideband radar is considered for W-STAP. In Section V, a 2D space-time keystone transform algorithm is proposed to address the problem of 2D clutter spreading, and hence improve the performance of W-STAP. Simulated data are employed to validate the proposed ST-KT algorithm. Finally, Section VI concludes this paper.

II. Signal Model of Single Clutter Sources for Airborne Array Radar

As mentioned by Ward [4], the echoes of the ground clutter can be modeled as the superposition of a large number of independent and discrete clutter sources evenly distributed in azimuth and elevation. In this section, we first establish the signal model of single clutter sources for airborne pulse-Doppler radar with an array antenna, which is then employed as a basis to investigate the influence of bandwidth to the space-time characteristics of the ground clutter. Note that, we do not hold any assumption on the bandwidth of radar, and here derive a generalized form to describe the echo signal of single ground clutter sources, which is suitable for different bandwidths.

A 3D geometry of data collection (Cartesian coordinate system) and its 2D top view are shown in Fig. 1 (a) and (b), respectively. The array system under consideration is a uniform linear array (ULA) that is horizontally oriented and parallel to X-axis. The airborne platform is at an altitude denoted by H and moving at a constant velocity denoted by v_a. The crab angle, defined to be the angle between the flight direction and the ULA axis, is represented by β.
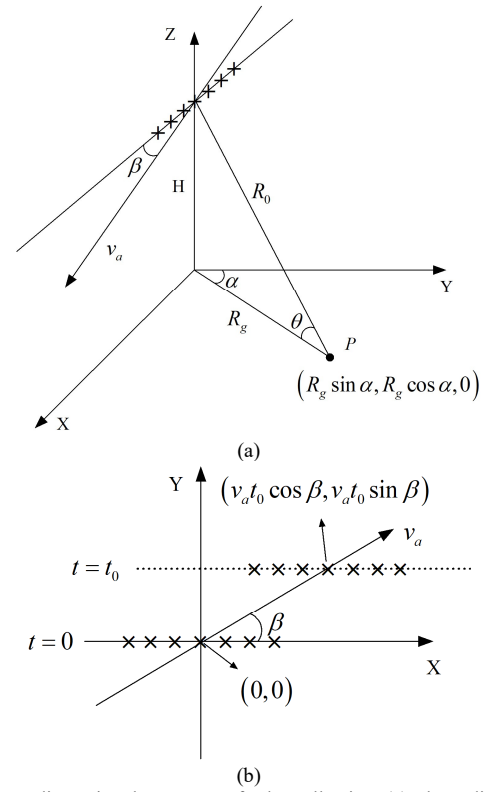

Fig. 1 Three-dimensional geometry of echo collection: (a) Three-dimensional geometry. (b) Top view of the array.

Let continuous variable t denote the slow-time, continuous variable η refer to the along-array position, i.e., the distance between the element under consideration and the reference element along the ULA axis (the element in the central position on the ULA is defined as the reference element in this paper), and assume that the coordinate of the reference element in the Cartesian coordinate system is $(0,0,H)$ when $t=0$. Thus, the instantaneous coordinate of each array element can then be represented as $(v_a \cos\beta t + \eta, v_a \sin\beta t, H)$.

Consider now that a stationary scatterer (single clutter source), denoted by P in Fig. 1 (a), is localized on the ground. Let R_0 represent the distance of P to the reference element, α and θ denote the azimuth and elevation angles of P with respect to the reference element, respectively, when $t=0$. The coordinate of P is then given by $(R_0 \cos\theta \sin\alpha, R_0 \cos\theta \cos\alpha, 0)$. Therefore, the instantaneous range from this clutter source to each array element is obtained from (see (1))

By expanding the above binary function in a Taylor series [39] about $(t,\eta)=(0,0)$, we have

$$R(t,\eta) = R(0,0) + R_t'(0,0)t + R_\eta'(0,0)\eta + \circ(t,\eta) \qquad (2)$$

where $R_t'(0,0)$ and $R_\eta'(0,0)$ are calculated from

$$R(t,\eta) = \sqrt{\left(v_a \cos\beta t + \eta - R_0 \cos\theta \sin\alpha\right)^2 + \left(v_a \sin\beta t - R_0 \cos\theta \cos\alpha\right)^2 + H^2} \; . \qquad (1)$$

$$R'_t(0,0) = \left.\frac{\partial R(t,\eta)}{\partial t}\right|_{(t,\eta)=(0,0)} \tag{3}$$

and

$$R'_\eta(0,0) = \left.\frac{\partial R(t,\eta)}{\partial \eta}\right|_{(t,\eta)=(0,0)} \tag{4}$$

respectively, with $\dfrac{\partial R(t,\eta)}{\partial t}$ and $\dfrac{\partial R(t,\eta)}{\partial \eta}$ denoting the first partial derivatives of $R(t,\eta)$ with respect to t and η, which are expressed as

$$\frac{\partial R(t,\eta)}{\partial t} = \frac{\left(v_a\cos\beta t + \eta - R_0\cos\theta\sin\alpha\right)v_a\cos\beta}{R(t,\eta)} \\ + \frac{\left(v_a\sin\beta t - R_0\cos\theta\cos\alpha\right)v_a\sin\beta}{R(t,\eta)} \tag{5}$$

and

$$\frac{\partial R(t,\eta)}{\partial \eta} = \frac{\left(v_a\cos\beta t + \eta - R_0\cos\theta\sin\alpha\right)}{R(t,\eta)} \tag{6}$$

respectively. $\circ(t,\eta)$ stands for the quadratic and higher order terms of the expansion. Substituting $(t,\eta)=(0,0)$ into Eqs. (5) and (6), and using Eq. (2), we have

$$R(t,\eta) = R_0 - \left[v_a\cos\theta\sin(\alpha+\beta)\right]t \\ - \left[\cos\theta\sin\alpha\right]\eta + \circ(t,\eta). \tag{7}$$

Note that, in general STAP implementations, the number of the pulses contained in one coherent processing interval (CPI) is relatively small, and the size of the array mounted on a moving platform is also limited, suggesting that both the distance travelled by the platform in one CPI and the length of ULA are far smaller than the distance between the clutter source and the radar. As a result, the quadratic and higher order terms in Eq. (7) is very small and hence can be ignored in the following discussion. Thus, the range equation in Eq. (7) can be substituted by the approximate expression given by

$$R(t,\eta) \approx R_0 - \left[v_a\cos\theta\sin(\alpha+\beta)\right]t - \left[\cos\theta\sin\alpha\right]\eta. \tag{8}$$

Without loss of generality, we consider here a traditional single-input and multiple-output (SIMO) working model for the array, and assume the position of the reference element is the phase center of the transmission. Thus, the two-way range history of the clutter source with respect to the array radar is given by

$$R_{TW}(t,\eta) = R(t,0) + R(t,\eta) \\ = 2R_0 - 2\left[v_a\cos\theta\sin(\alpha+\beta)\right]t - \left[\cos\theta\sin\alpha\right]\eta. \tag{9}$$

The full array transmits a series of pulses and each of the elements receives echo signal independently. After down-conversion and pulse compression, the baseband echo signal from the clutter source received by the ULA can be represented as

$$s_R(\tau,t,\eta) = A_1 s_c\left[\tau - \frac{R_{TW}(t,\eta)}{c}\right]\exp\left[\frac{-j2\pi f_c R_{TW}(t,\eta)}{c}\right] \tag{10}$$

where $s_c(\tau)$ denotes the waveform of the transmitted signal after pulse compression (point spread function), with the variable τ denoting the fast-time, f_c is the carrier frequency of the radar, A_1 is a constant depending on the radar cross section (RCS) of the scatterer, and c is the speed of light. By defining

$$\phi(t,\eta) = \frac{-2\pi f_c R_{TW}(t,\eta)}{c} \tag{11}$$

to be the phase of Eq. (10) whilst omitting the constant amplitude A_1, we can rewrite Eq. (10) in a simplified formation as follows:

$$s_R(\tau,t,\eta) = s_c\left[\tau - \frac{R_{TW}(t,\eta)}{c}\right]e^{j\phi(t,\eta)}. \tag{12}$$

Thus, the echo signal of the clutter source is actually comprised of two terms, which are represented by

$$s_1(\tau,t,\eta) = s_c\left[\tau - \frac{R_{TW}(t,\eta)}{c}\right] \tag{13}$$

and

$$s_2(t,\eta) = e^{j\phi(t,\eta)} \tag{14}$$

respectively. The first term, i.e., $s_1(\tau,t,\eta)$, reveals the variation in the fast-time delays of the point spread function between the pulses and the array elements. The variation of the delays dependent on slow-time is also known as range migration (RM) in the field of synthetic aperture radar (SAR) [40] and the variation of the delays across the array is referred to as aperture fill (AF) in wideband array processing [25]. The second term, i.e., $s_2(t,\eta)$, stands for the phase history of the echo signal, and is independent on fast-time. In this paper, we refer the first and second terms of Eq. (12) as the RM term and phase history term for simplification.

Substituting Eq. (9) into (11), and omitting the constant term induced by R_0, we obtain

$$\phi(t,\eta) = \frac{4\pi f_c}{c}\left[v_a\cos\theta\sin(\alpha+\beta)\right]t + \frac{2\pi f_c}{c}\left(\cos\theta\sin\alpha\right)\eta. \tag{15}$$

By defining

$$F_d(\alpha,\theta) = \frac{2f_c}{c}\left[v_a\cos\theta\sin(\alpha+\beta)\right] \tag{16}$$

and

$$F_s(\alpha,\theta) = \frac{f_c}{c}\left(\cos\theta\sin\alpha\right) \tag{17}$$

to be the Doppler frequency and spatial frequency with respect to the clutter source localized at (α,θ), $s_2(t,\eta)$ can then be expressed as

$$s_2(t,\eta) = e^{j2\pi F_d(\alpha,\theta)t}e^{j2\pi F_s(\alpha,\theta)\eta}. \tag{18}$$

Note that, Eq. (18) is just the basic signal model utilized in the traditional narrowband STAP theory [2, 4-6], where the echo signal from each clutter source is recognized as a 2D single-frequency signal in the space-time domain.

Let m and n denote the indexes of pulses and array elements, respectively, M and N stand for the total numbers of pulses and elements, respectively, f_{PRF} represent the pulse repetition frequency (PRF), and d denote the inter-element distance of the ULA. The discrete form of $s_2(t, \eta)$ is then given by

$$s_2(n, m) = e^{jm 2\pi \bar{F}_d(\alpha, \theta)} e^{jn 2\pi \bar{F}_s(\alpha, \theta)}$$
$$m = 1, 2, \ldots, M, \ n = 1, 2, \ldots, N \tag{19}$$

where

$$\bar{F}_d(\alpha, \theta) = \frac{F_d(\alpha, \theta)}{f_{PRF}} \tag{20}$$

and

$$\bar{F}_s(\alpha, \theta) = F_s(\alpha, \theta) d \tag{21}$$

are referred to as the normalized Doppler and normalized spatial frequencies, which have already been defined in the literature [4-6]. By introducing the notation of the matrix, Eq. (19) can also be rewritten in a vector form referred to as space-time steering vector with respect to clutter path (α, θ) in the literature, which is given by [2-6]

$$\mathbf{s}_2(\alpha, \theta) = \mathbf{s}_T(\alpha, \theta) \otimes \mathbf{s}_S(\alpha, \theta) \tag{22}$$

where

$$\mathbf{s}_T(\alpha, \theta) = \left[e^{j2\pi \bar{f}_d(\alpha, \theta)}, e^{j4\pi \bar{f}_d(\alpha, \theta)}, \ldots, e^{jM 2\pi \bar{f}_d(\alpha, \theta)} \right]^T \tag{23}$$

and

$$\mathbf{s}_S(\alpha, \theta) = \left[e^{j2\pi \bar{f}_s(\alpha, \theta)}, e^{j4\pi \bar{f}_s(\alpha, \theta)}, \ldots, e^{jN 2\pi \bar{f}_s(\alpha, \theta)} \right]^T \tag{24}$$

are the steering vectors in the temporal and spatial domains, respectively, $\otimes$ stands for the Kronecker product, and superscript T denotes the operation of transposition.

We now turn our attention to the RM term. Without loss of generality, we assume the transmitted signal in each pulse is a linear frequency modulation (LFM) signal (which is widely used in airborne pulse-Doppler radar, and also referred to as chirp signal) given by

$$s_{LFM}(t) = \text{rect}\left[\frac{t}{T_p} \right] \exp\left(-j \frac{B}{T_p} \pi t^2 \right) \tag{25}$$

where T_p and B are the pulse length and bandwidth of the LFM signal, respectively. Assuming that there is no additional window (taper) function used in the procedure of the pulse compression, $s_1(\tau, t, \eta)$ can be denoted by the following sinc function

$$s_1(\tau, t, \eta) = A_2 \text{sin} c \left[B\left(\tau - \frac{R_{TW}(t, \eta)}{c} \right) \right] \tag{26}$$

where A_2 is a constant that depends on different methods used for pulse compression. Substituting Eqs. (9), (16), and (17) into (26) and omitting constant A_2, we obtain

$$s_1(\tau, t, \eta) = \text{sin} c \left\{ B\left(\tau - \frac{2R_0}{c} \right) + \frac{B}{f_c} \left[F_d(\alpha, \theta)t + F_s(\alpha, \theta)\eta \right] \right\}. \tag{28}$$

By introducing the discrete forms of variable t and η, $s_1(\tau, t, \eta)$ can also be expressed as a column vector given by

$$\mathbf{s}_1(\tau, \alpha, \theta) = \begin{bmatrix} \text{sin} c \left\{ B\left(\tau - \frac{2R_0}{c} \right) + \frac{B}{f_c} \left[\bar{f}_d(\alpha, \theta) + \bar{f}_s(\alpha, \theta) \right] \right\} \\ \vdots \\ \text{sin} c \left\{ B\left(\tau - \frac{2R_0}{c} \right) + \frac{B}{f_c} \left[\bar{f}_d(\alpha, \theta) + N\bar{f}_s(\alpha, \theta) \right] \right\} \\ \text{sin} c \left\{ B\left(\tau - \frac{2R_0}{c} \right) + \frac{B}{f_c} \left(2\bar{f}_d(\alpha, \theta) + \bar{f}_s(\alpha, \theta) \right) \right\} \\ \vdots \\ \text{sin} c \left\{ B\left(\tau - \frac{2R_0}{c} \right) + \frac{B}{f_c} \left[M\bar{f}_d(\alpha, \theta) + N\bar{f}_s(\alpha, \theta) \right] \right\} \end{bmatrix} \tag{29}$$

Thus, the vector form of the echo signal (the space-time steering vector) from the clutter source localized at (α, θ) can be expressed as the Hadamard product of Eqs. (28) and (22), which is given by

$$\mathbf{s}_R(\tau, \alpha, \theta) = \mathbf{s}_1(\tau, \alpha, \theta) \odot \mathbf{s}_2(\alpha, \theta) \tag{30}$$

where $\odot$ stands for the Hadamard product. Now, substituting Eqs. (27) and (18) into (12), the continuous form of the echo signal is obtained (see (30)):

From the above formulas, it is clear that the difference between the signal model used in the traditional narrowband STAP and the general model given by Eqs. (29) and (30) mainly lies in the RM term. In the traditional STAP theory, the RM term is not considered because it varies slightly between pulses and across the array when the bandwidth is relatively small. However, when the bandwidth increases, the RM is enlarged, leading to the decorrelation in both temporal and spatial domains.

Based on the signal model provided by Eq. (29) as well as its continuous form in Eq. (30), we will present thorough discussion on the influence of bandwidth onto the space-time characteristics of single clutter sources in the next section.

III. THE INFLUENCE OF BANDWIDTH ON SPACE-TIME CHARACTERISTICS OF SINGLE CLUTTER SOURCES

In this section, the influence of bandwidth on the space-time characteristics of single clutter sources is investigated in detail. As discussed in the previous section, the major difference between the signal model presented in this paper and that in the traditional STAP theory is the RM term. So it can be deduced

$$s_R(\tau, t, \eta) = \text{sin} c \left\{ B\left(\tau - \frac{2R_0}{c} \right) + \frac{B}{f_c} \left[F_d(\alpha, \theta)t + F_s(\alpha, \theta)\eta \right] \right\} e^{j2\pi F_d(\alpha, \theta)t} e^{j2\pi F_s(\alpha, \theta)\eta}. \tag{27}$$

that the RM within the snapshot is a key factor affecting the space-time characteristics of the ground clutter. Consequently, we now turn our attention to the RM term and investigate how it affects the 2D spectrum of the single clutter sources in case of wideband.

In the following two subsections, the characteristics of the RM term is analyzed in the fast-time and fast-time frequency (range frequency) domains, respectively, and quantitative results to evaluate the 2D spectrum spreading of single clutter sources are also presented.

3.1 Analysis in the Fast-Time Domain

Using the Fourier property, the multiplication of $s_1(\tau, t, \eta)$ and $s_2(t, \eta)$ shown in Eq. (18) is equivalent to the 2D convolution in the 2D frequency domain (the Doppler-spatial frequency domain) given by

$$S_R(\tau, f_d, f_s) = S_1(\tau, f_d, f_s) \otimes S_2(f_d, f_s) \qquad (31)$$

where $S_1(\tau, f_d, f_s)$ and $S_2(f_d, f_s)$ are the 2D spectra of $s_1(\tau, t, \eta)$ and $s_2(t, \eta)$, i.e., the 2D Fourier transforms (2D-FT) to $s_1(\tau, t, \eta)$ and $s_2(t, \eta)$ with respect to t and η, respectively, $S_R(\tau, f_d, f_s)$ is the 2D spectrum of the clutter source, variables f_d and f_s are used to identify the Doppler and spatial frequencies, respectively, and $\otimes$ stands for the operation of 2D convolution. Considering that $s_2(t, \eta)$ is a single-frequency signal in the space-time domain, the 2D-FT of $s_2(t, \eta)$ is given by

$$S_2(f_d, f_s) = \delta_{2D}\left[f_d - F_d(\alpha, \theta), f_s - F_s(\alpha, \theta)\right] \qquad (32)$$

where $\delta_{2D}[f_d, f_s]$ is the 2D impulse function in 2D frequency domain. Substituting Eq. (32) into (31), the 2D spectrum of the clutter source localized at (α, θ) is obtained from

$$S_R(\tau, f_d, f_s) = S_1\left[\tau, f_d - F_d(\alpha, \theta), f_s - F_s(\alpha, \theta)\right]. \qquad (33)$$

As we can see, the 2D spectrum of the clutter source is equivalent to the displayed spectrum of the RM term. Appling a 2D-FT to Eq. (27) with respect to t and η, we obtain the 2D spectrum of $s_1(\tau, t, \eta)$

$$S_1(\tau, f_d, f_s) = \frac{f_c F_d(\alpha, \theta)}{B} rect\left[\frac{f_d}{\left(\frac{BF_d(\alpha, \theta)}{f_c}\right)}\right]$$

$$\cdot \delta\left[f_s - \frac{F_s(\alpha, \theta)}{F_d(\alpha, \theta)} f_d\right] e^{j2\pi \frac{\left(\tau - \frac{2R_0}{c}\right) f_c}{F_d(\alpha, \theta)} f_d} \qquad (34)$$

where $\delta[\cdot]$ is the 1D impulse function (delta function), and $rect[\cdot]$ denotes the rectangular function. Considering that the

constant term, i.e., $\dfrac{f_c F_d(\alpha, \theta)}{B}$, and the exponential term, i.e.,

$e^{j2\pi \frac{\left(\tau - \frac{2R_0}{c}\right) f_c}{F_d(\alpha, \theta)} f_d}$, will not affect the shape of $S_1(\tau, f_d, f_s)$, we omit these terms for simplification and rewrite Eq. (34) as follows:

$$S_1(f_d, f_s) \approx rect\left[\frac{f_d}{\left(\frac{BF_d(\alpha, \theta)}{f_c}\right)}\right] \delta\left[f_s - \frac{F_s(\alpha, \theta)}{F_d(\alpha, \theta)} f_d\right]. \qquad (35)$$

The above formula that denotes the shape of $S_1(f_d, f_s)$ allows us to quantitatively describe the spectrum spreading of the clutter source. The impulse function, with its peaks ($\delta[0]$) localized along the line denoted by

$$f_s = \frac{F_s(\alpha, \theta)}{F_d(\alpha, \theta)} f_d \qquad (36)$$

on the 2D f_d - f_s plane, indicates the direction of spectrum spreading, and the rectangular function defines the range of spreading, which is given by

$$-\frac{BF_d(\alpha, \theta)}{2f_c} < f_d < \frac{BF_d(\alpha, \theta)}{2f_c}. \qquad (37)$$

Hence, we observe that the spectrum spreading of the clutter source can be exactly described by a line segment on the f_d-f_s plane, where the slope is determined by the ratio of the spatial frequency to the Doppler frequency of the clutter source, and the length is proportional to the radar bandwidth.

We now show examples to support the above discussions and to compare the spectrum spreading in cases of narrowband and wideband. The major parameters used for this simulation are listed in Table I, and two different bandwidths, i.e., 10MHz and 240MHz, are chosen for the cases of narrowband and wideband, respectively.

TABLE I
PARAMETERS OF THE SPACE-TIME SPECTRUM SIMULATION

Parameter	Value
Carrier frequency	1GHz
Bandwidth	10MHz/240MHz
Platform speed	75m/s
Crab angle	20°
PRF	1000Hz
Number of array elements	32
Number of coherent processing pulses	32
Inter-element distance of the ULA	Half-wavelength
Elevation of the clutter source	30°
Azimuth of the clutter source	45°
Distance between the clutter source and radar	15km

In Fig. 2, the characteristics of the RM term in both the space-time and 2D frequency domains are demonstrated. We first consider the case of narrowband and set the bandwidth to be 10MHz. The amplitude of the RM term in the space-time domain is shown in Fig. 2 (a). As can be seen, for relatively small bandwidth, the amplitude of RM varies slightly within the

snapshot (see the values on the color-bar), implying that the data are strongly correlated across pulses and also across elements. Appling a 2D fast Fourier transform (FFT) to the RM
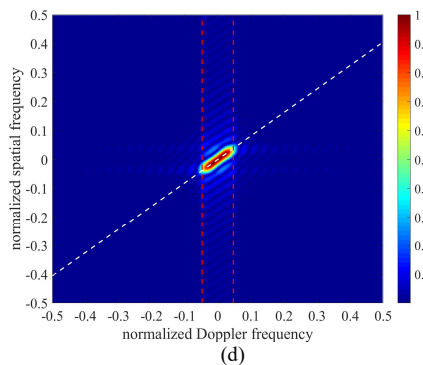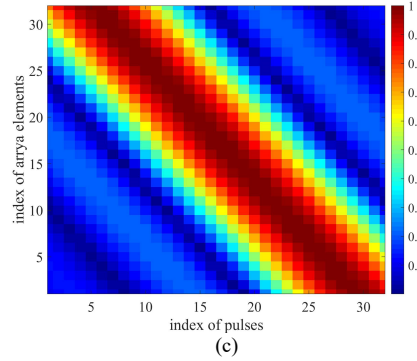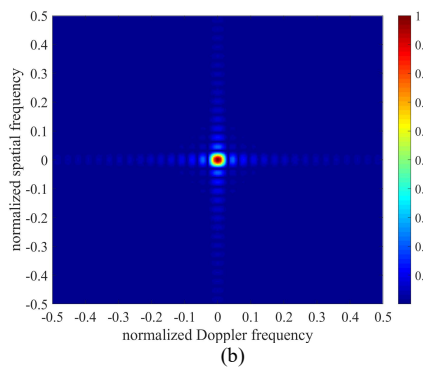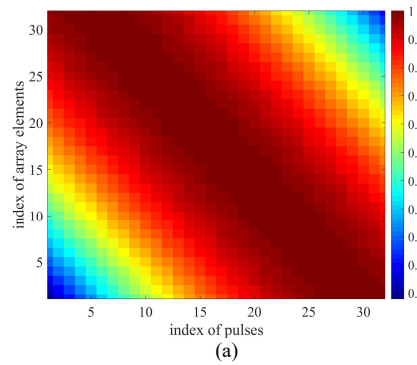

(a)

(b)

(c)

(d)

Fig. 2 Demonstrations of RM in the space-time and 2D frequency domains with different bandwidths. (a) RM in space-time domain when the bandwidths is equal to 10MHz. (b) RM in the 2D frequency domain when the bandwidths is equal to 10MHz. (c) RM in space-time domain when the bandwidths is equal to 240MHz. (d) RM in the 2D frequency domain when the bandwidths is equal to 10MHz.

term shown in Fig. 2 (a), the 2D spectrum is obtained and displaced in Fig. 2 (b), where no evident spectrum spreading is recognized. The bandwidth is then set to be 240MHz to simulate the case of wideband, and the relevant results are displaced in Fig. 2 (c) and (d). As we can see from Fig. 2 (c), the amplitude of the RM term varies more significantly as compared to that of Fig. 2 (a), leading to considerable decorrelation within the snapshot. As a result, the 2D spectrum of the RM term spreads in the 2D frequency domain, which is clearly seen from Fig. 2 (d). To validate the quantitative analysis on the spectrum spreading of the RM term, the straight line denoted by Eq. (36) and the upper and lower bounds denoted by Eq. (37) are also plotted in Fig. 2 (d). The white dash line stands for Eq. (36) and the pair of red dash lines shows the bounds in Eq. (37). As we can see, positions of the lines and the locus of the 2D spectrum is highly corresponding, which directly validates the above quantitative analysis on the spectrum spreading of the RM term.

In Fig. 3, the final 2D spectra of the clutter source in cases of narrowband and wideband are displayed in Fig. 3 (a) and (b), respectively. As we can see, the spectrum spreading in case of wideband is more evident as compared to the case of narrowband. We also note that, the two subfigures are actually the displaced spectra of the RM term shown in Fig. 2 (b) and (d). Hence, it is clear that the spectrum spreading of the clutter source is fully determined by the RM term.
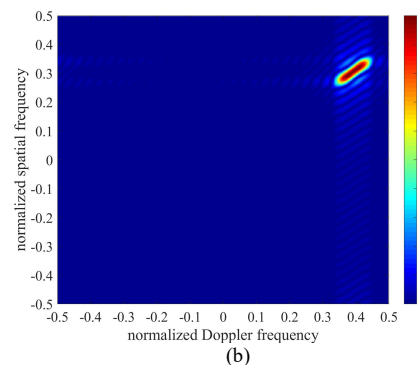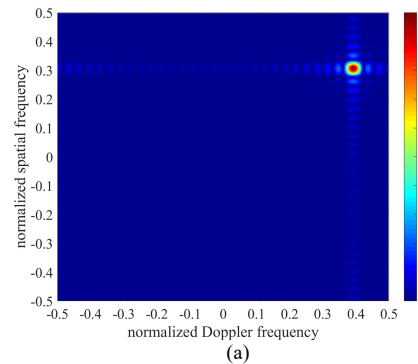

(a)

(b)

Fig. 3 Two-dimensional spectra of the clutter source with different bandwidths. (a) The bandwidth is 10MHz. (b) The bandwidth is 240MHz.

3.2 Analysis in the Fast-time Frequency Domain

In this subsection, the characteristics of the RM term as well as the spectrum spreading of single clutter sources are analyzed in the fast-time frequency (range frequency) domain. Applying

a FT transform to Eq. (27) with respect to τ, the RM term in the fast-time frequency domain is obtained from

$$S_1\left(f_r,t,\eta\right) = A_3 rect\left[\frac{f_r}{B}\right]\exp\left[\frac{-j2\pi R_0 f_r}{c}\right]$$
$$\cdot\exp\left\{\frac{j2\pi\left[F_d\left(\alpha,\theta\right)+F_s\left(\alpha,\theta\right)\right]f_r}{f_c}\right\} \quad (38)$$

where variable f_r is used to identify the fast-time frequency, and A_3 is also a constant. Then, we define

$$\Delta F_d\left(f_r,\alpha,\theta\right) = \frac{f_r}{f_c}F_d\left(\alpha,\theta\right) \quad (39)$$

and

$$\Delta F_s\left(f_r,\alpha,\theta\right) = \frac{f_r}{f_c}F_s\left(\alpha,\theta\right) \quad (40)$$

to be the fast-time frequency dependent changes of Doppler and spatial frequencies. Substituting Eqs. (39) and (40) into (38), and omitting constant A_3 and the exponential term $\exp\left[\frac{-j2\pi R_0 f_r}{c}\right]$ denoting the constant time-delay, we obtain

$$S_1\left(f_r,t,\eta\right) = rect\left[\frac{f_r}{B}\right]$$
$$\cdot\exp\left\{j2\pi\left[\Delta F_d\left(f_r,\alpha,\theta\right)t + \Delta F_s\left(f_r,\alpha,\theta\right)\eta\right]\right\} \quad (41)$$

Multiplying Eq. (41) by (18), the received signal in the fast-time frequency domain is expressed as

$$S_R\left(f_r,t,\eta\right) = rect\left[\frac{f_r}{B}\right]$$
$$\cdot e^{j2\pi\left[F_d\left(\alpha,\theta\right)+\Delta F_d\left(f_r,\alpha,\theta\right)\right]t}e^{j2\pi\left[F_s\left(\alpha,\theta\right)+\Delta F_s\left(f_r,\alpha,\theta\right)\right]\eta} \quad (42)$$

Comparing Eq. (42) with (18), we find that the RM term induces additional Doppler and spatial frequencies to the traditional 2D single-frequency signal, and the additional frequencies depend on the fast-time frequency f_r. Consequently, when transferred back to the fast-time domain, the 2D spectrum of the echo signal spreads. Dividing Eq. (39) by (40), the coupling relationship between the changes of Doppler and spatial frequencies can be acquired from

$$\Delta F_s\left(f_r,\alpha,\theta\right) = \frac{F_s\left(\alpha,\theta\right)}{F_d\left(\alpha,\theta\right)}\Delta F_d\left(f_r,\alpha,\theta\right). \quad (43)$$

Considering the rectangular function in Eq. (41), the range of f_r is given by

$$-\frac{B}{2} < f_r < \frac{B}{2}. \quad (44)$$

Substituting Eq. (39) in to (44) yields the range of $\Delta F_d\left(f_r,\alpha,\theta\right)$

$$-\frac{BF_d\left(\alpha,\theta\right)}{2f_c} < \Delta F_d\left(f_r,\alpha,\theta\right) < \frac{BF_d\left(\alpha,\theta\right)}{2f_c}. \quad (45)$$

From Eqs. (43) and (45), the RM term induced additional Doppler and spatial frequencies have the coupled relationship that can be described by a line segment on the f_d-f_s plane.

We also note that, the slope in Eq. (43) and the boundary given by Eq. (45) are exactly identical with that shown in Eqs. (36) and (37), which again verifies the quantitative analysis on the 2D spectrum spreading of the single clutter sources.

We also use another similar example to validate the above discussion in the fast-time frequency domain. All the related parameters are the same as that illustrated in Table I. In Fig.4, the centers of the 2D spectrum of the clutter source on different fast-time frequencies are marked by circles with different colors. As we can see, the 2D spectrum of the clutter source varies with the fast-time frequency, indicating that the 2D spectrum within the snapshot spreads in the 2D frequency domain. We also note that, Fig. 4 is in accordance with the 2D spectrum of the clutter source shown in Fig. 3 (b).
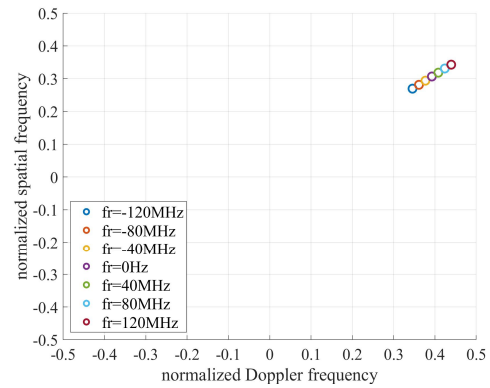

Fig. 4 Centers of the 2D spectrum of the clutter source on different fast-time frequencies.

From the above discussions on the 2D spectrum of single clutter sources, we witness that the RM within the snapshot, which is assumed to be negligible in the traditional STAP theory, is the major aspect that induces the 2D spectrum spreading of the ground clutter, when the radar bandwidth increases.

IV. SPACE-TIME CHARACTERISTICS OF GROUND CLUTTER FOR WIDEBAND RADAR

For airborne surveillance radar working on the air-to-ground mode, the ground surface is the major source of clutter. Of all the components of interference, ground clutter is one of the most complicated factors, which is distributed in both Doppler and spatial frequencies domains. As it has been mentioned in the literature [30, 31], obvious spectrum spreading in the 2D frequency domain for the ground clutter is observed in case of wideband. The spectrum spreading of the ground clutter makes the clutter suppressing notch of the adaptive filter broader than the corresponding narrowband case, and thereby degrades the slow-moving target detection ability of the STAP methods.

In this section, based on the signal model presented in Section II, a generalized model is developed for ground clutter in the space-time snapshot for a given range gate, when a wideband radar is considered. Based on this analysis, the covariance matrix for the ground clutter in case of wideband is established, which enables us to investigate the influences of bandwidth on the space-time characteristics of the ground clutter. Note that, since we only focus on the influences of

bandwidth onto STAP in this paper, the clutter model presented here is a generalized model, where other factors, such as intrinsic clutter motion, range ambiguity, and imbalance of receiving channels, are not considered herein. In addition, we also assume that the ground is flat, which is acceptable for airborne radar [2,4].

In the Cartesian coordinate system defined in Fig. 1, the position of any discrete clutter source on the ground is described by its azimuth and elevation angles, i.e., α and θ. Since ground clutter is distributed in both the two directions on the ground, theoretically, clutter sources localized at all the azimuth and elevation angles will contribute to the received echo signals. The final clutter component consists of the superposition of echoes from all the azimuths and elevations. Consequently, the clutter vector in the space-time snapshot at the range gate with respect to fast-time τ can be denoted by the following two-fold integral

$$\chi_c(\tau) = \int_\alpha \int_\theta c(\alpha,\theta)\mathbf{s}(\tau,\alpha,\theta)d\theta d\alpha \tag{46}$$

where $c(\alpha,\theta)$ is the amplitude of the clutter source localized at (α,θ). For convenience, an approximation to the continuous field of clutter shown in Eq. (46) is constructed, in which the clutter return in each snapshot is modeled as the superposition of a large number of discrete independent clutter sources evenly distributed in both azimuth and elevation angles. Letting i and k denote the indexes of the discrete azimuth and elevation locations, the azimuth and elevation locations of the (i,k)th clutter source are described by α_i and θ_k, and the amplitude is denoted by $c_{i,k}$. Thus, we obtain the discrete form expression of Eq. (46), which is given by

$$\chi_c(\tau) = \sum_i^{N_a} \sum_k^{N_e} c_{i,k}\mathbf{s}(\tau,\alpha_i,\theta_k) \tag{47}$$

where N_a and N_e are the total numbers of clutter sources in azimuth and elevation.

Assuming that the echoes from different clutter sources are uncorrelated (a common assumption in research field of STAP [2-6]), the space-time covariance matrix of $\chi_c(\tau)$ is then given by

$$\mathbf{R}_c(\tau) = E\left[\chi_c(\tau)\chi_c^H(\tau)\right] = \sum_i^{N_a}\sum_k^{N_e}\sigma_{c,i,k}^2\mathbf{s}(\tau,\alpha_i,\theta_k)\mathbf{s}^H(\tau,\alpha_i,\theta_k) \tag{48}$$

where

$$\sigma_{c,i,k}^2 = E\left[c_{i,k}c_{i,k}^*\right] \tag{49}$$

with $E[\cdot]$ denoting the expectation operator, is the power of the (i,k)th clutter source. Introducing Eq. (29) into (48), we obtain the final clutter covariance matrix as follows:

$$\mathbf{R}_c(\tau) = \sum_i^{N_a}\sum_k^{N_e}\left\{\sigma_{c,i,k}^2\left[\mathbf{s}_1(\tau,\alpha_i,\theta_k)\mathbf{s}_1^H(\tau,\alpha_i,\theta_k)\right]\right.$$
$$\left. \odot\left[\mathbf{s}_2(\alpha_i,\theta_k)\mathbf{s}_2^H(\alpha_i,\theta_k)\right]\right\} \tag{50}$$

By comparing Eq. (50) to the expression of the clutter

covariance matrix used in the narrowband STAP [4], it is clear that the difference lies in the additional matrix generated by the self-exterior product of the RM vector for each clutter source, i.e., $\mathbf{s}_1(R,\alpha_i,\theta_k)\mathbf{s}_1^H(R,\alpha_i,\theta_k)$. As discussed in Section III, the RM term leads to additional spreading of the 2D spectrum of single clutter source along the line defined by Eq. (36) on the 2D f_d-f_s plane. Thus, each clutter source will spread along different directions in the 2D frequency domain, leading to the spreading of the entire clutter spectrum.

In Fig. 5, the spectrum spreading of a group of clutter sources are shown. All the clutter sources are localized at an identical elevation angle ($30°$), but distributed in different azimuth positions. The total number of the clutter sources is 17, and the azimuth positions of them are set to be $[-80°,-70°,\ldots,70°,80°]$. All the other relevance parameters are the same as those shown in Table I. As we can see, since the clutter sources localized at different azimuth positions have different central Doppler and spatial frequencies, the spreading of them in the 2D frequency domain differ from each other.
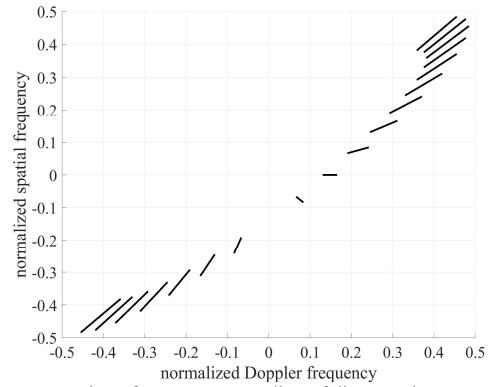

Fig. 5 Demonstration of spectrum spreading of discrete clutter sources from different azimuths.

In Fig. 6, the 2D minimum variance distortionless response (MVDR) spectra of the ground clutter in cases of wideband and narrowband are provided, where the 2D spreading of clutter spectrum caused by increasing bandwidth is clearly seen. The parameters employed here are the same as those listed in Table I. To clearly show the entire spectra of the ground clutter from all the azimuth directions, a cosine-shape antenna pattern is assumed, but the back lobe of the antenna is ignored. By comparing the two MVDR spectra, it is obvious that the spectrum of the ground clutter spreads, in both Doppler and spatial frequencies, when the bandwidth of radar increases. Moreover, the shape of the spectrum shown in Fig. 6 (a) is in accordance with the demonstration of discrete clutter sources shown in Fig. 5.

In Fig. 7, the ranks of the ground clutter in cases of wideband and narrowband are tested via the eigenspectra of the ground clutter. As we can see, instead of the "cliff-like" eigenspectrum in case of narrowband (10MHz), the spread clutter in case of wideband (240MHz) generates a smoother "slope-like" eigenspectrum. That means the rank of the ground clutter is enlarged when the radar bandwidth increases, which may degrade the performance of reduced-rank and reduced-
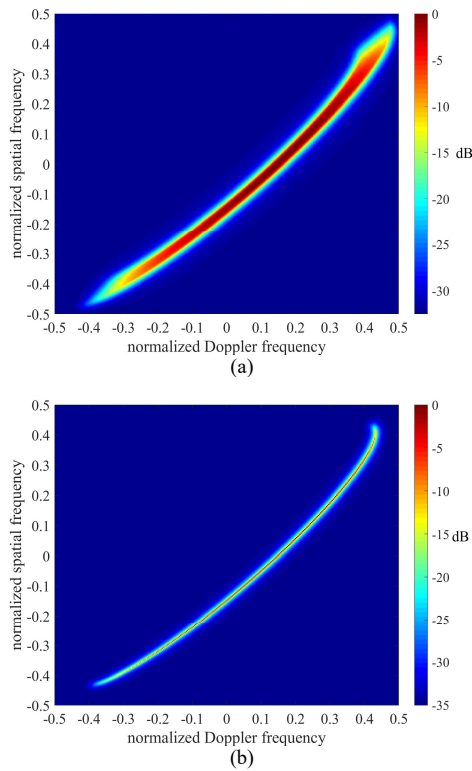
Fig. 6 Space-time MVDR spectra of the ground clutter with different bandwidths. (a) The radar bandwidth is 240MHz. (b) The radar bandwidth is 10MHz.
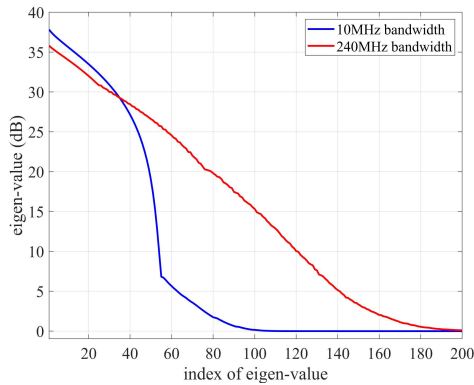

Fig. 7 Eigenspectra of the ground clutter with different bandwidths.

dimension STAP algorithms [8-12], such as joint domain localized (JDL) STAP [9], eigen-canceller [10], and the like.

Fig. 8 compares the performance of the traditional STAP methods in cases of wideband and narrowband by the calculated signal-to-clutter plus noise ratio (SCNR) loss. The SCNR loss of a STAP algorithm is defined as the output SCNR relative to the output signal-to-noise ratio (SNR) of the matched filter in an interference-free environment, which is given by [2, 4]

$$L_{SCNR}\left(f_d,f_s\right) = \frac{1}{MN} \frac{\left|\mathbf{w}^H\left(f_d,f_s\right)\mathbf{v}\left(f_d,f_s\right)\right|^2}{\mathbf{w}^H\left(f_d,f_s\right)\mathbf{R}\mathbf{w}\left(f_d,f_s\right)}. \qquad (51)$$

where $\mathbf{v}\left(f_d,f_s\right)$ is the space-time steering vector for the moving target with Doppler and spatial frequencies equal to f_d and f_s, respectively, $\mathbf{R}$ is the clutter-plus-noise covariance

matrix, and $\mathbf{w}\left(f_d,f_s\right)$ is the adaptive weight corresponding to Doppler frequency f_d and spatial frequency f_s. In this paper, all the SCNR loss curves are corresponding to the boresight direction of the beam ($f_s=0$). In Fig. 8 (a), the performance of the optimum STAP filter is tested, while in Fig. 8 (b), the performance of a classical reduced-dimension STAP algorithm, i.e., the 3×3 JDL-STAP algorithm [10], is evaluated. As we can see from these curves, the clutter suppressing notch in case of wideband for each of the fully and partial optimum STAP algorithm is much broader than that of the corresponding narrowband case, implying that the current STAP algorithms have a worse slow-moving target detection ability when the radar bandwidth increases.
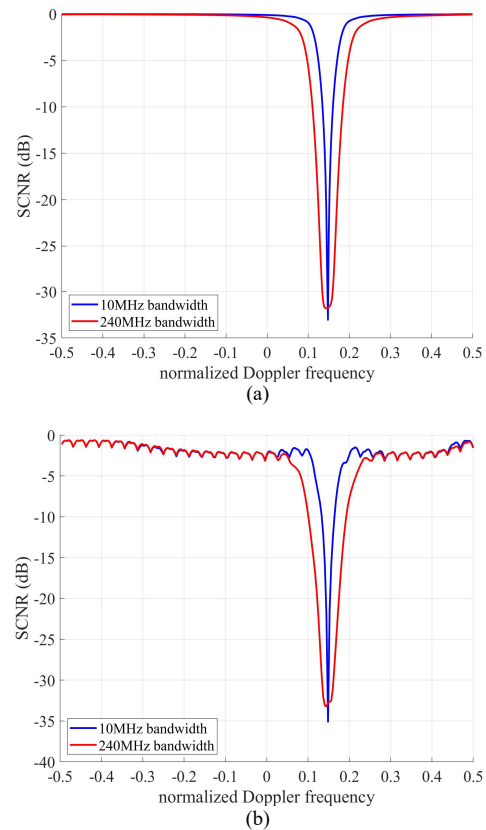

Fig. 8 SCNR loss curves with different bandwidths. (a) Optimum SCNR curves. (b) SCNR curves obtained via 3×3 JDL algorithm.

V. Two-Dimensional Space-Time Keystone Transform for W-STAP

Compared to narrowband radar, the slow-moving target detection performance for wideband array radar degrades when using the traditional STAP methods due to the spreading clutter spectrum in both Doppler and spatial frequencies domains. As discussed in the previous sections, the difference between the clutter model used in traditional narrowband STAP and that proposed in this paper is the RM term. We also deduced that the RM term is the major reason for the 2D spreading of the ground clutter in case of wideband. Therefore, how to eliminate the RM

term in the echo signals or to greatly reduce its influences becomes a key issue for W-STAP.

As we have mentioned in Section I, most of the current W-STAP methods use the sub-band processing approach or the 3D adaptive processing approach to reduce the impact induced by increasing bandwidth. However, both of them have certain drawbacks such as heavy computational burden and performance loss caused by mismatches between sub-bands, limiting their applications in practice. In this section, we present a 2D space-time keystone transform (ST-KT) algorithm, which is expected to thoroughly eliminate the RM term within each snapshot, and make the narrowband assumption revalidated.

5.1 Two-Dimensional Space-Time Keystone Transform

The keystone transform (KT) is well known as a classical method in the field of synthetic aperture radar (SAR) imaging, especially for SAR imaging of moving targets [41, 42]. It is widely used because its ability to compensate arbitrary linear range mitigations for moving targets or ground stationary scatterers, without the a priori information of target motion. The key step in the initial version of KT is a one dimension (1D) interpolation to rescale the slow-time axis for each fast-time frequency, which eliminates the range-Doppler coupling effect and hence removes the linear RM in the received signals.

With the capability of KT in mind, and based on our analysis on the RM in the range frequency domain (see Subsection 3.2), we now extend the traditional 1D KT into the 2D space-time domain to remove the linear RM term in both the slow-time and spatial domains from the received datacube. Substituting Eqs. (39) and (40) into (42), we rewrite the expression of the received data in the range frequency domain as

$$S_R(f_r, t, \eta) = rect\left[\frac{f_r}{B}\right]$$
$$\cdot \exp\left\{j2\pi \frac{f_r + f_c}{f_c} F_d(\alpha, \theta) t\right\}. \qquad (52)$$
$$\cdot \exp\left\{j2\pi \frac{f_r + f_c}{f_c} F_d(\alpha, \theta) t\right\}$$

As we can see from the two exponential terms, i.e.,

$$\exp\left\{j2\pi \frac{f_r + f_c}{f_c} F_d(\alpha, \theta) t\right\} \qquad \text{and}$$

$$\exp\left\{j2\pi \frac{f_r + f_c}{f_c} F_s(\alpha, \theta) \eta\right\}, \text{ because of the RM term, the}$$

Doppler and spatial frequencies of the clutter source vary with the range frequency, implying a coupling effect between the range frequency, slow-time, and along-array position. Specifically, the term $\exp\left\{j2\pi \frac{f_r + f_c}{f_c} F_d(\alpha, \theta) t\right\}$ represents the coupling between the range frequency and slow-time, and the term $\exp\left\{j2\pi \frac{f_r + f_c}{f_c} F_s(\alpha, \theta) \eta\right\}$ denotes the coupling between the range frequency and along-array position. When we transform the data back to the fast-time domain, this

coupling effect induces the spreading of the ground clutter in both Doppler and spatial frequency domains.

To eliminate this coupling effect, we propose to rescale the slow-time axis and the along-array position axis for each range frequency by the following 2D transform

$$\begin{cases} t = \dfrac{(f_r + f_c)}{f_c} \tilde{t} \\ \eta = \dfrac{(f_r + f_c)}{f_c} \tilde{\eta} \end{cases} \qquad (53)$$

where $\tilde{t}$ and $\tilde{\eta}$ are new variables of the rescaled slow-time and the along-array position, respectively. Substituting Eq. (53) into (52), we obtain

$$S_R(f_r, \tilde{t}, \tilde{\eta}) = rect\left[\frac{f_r}{B}\right]\exp\left\{j2\pi\left[f_d(\alpha, \theta)\tilde{t} + f_s(\alpha, \theta)\tilde{\eta}\right]\right\}.$$
$$(54)$$

It is clear that, the 2D transform in Eq. (52) decouples the range frequency and slow-time, and also the range frequency and along-array position, transforming the received signal to be signal-frequency in the space-time domain. Transforming Eq. (54) back to the range domain, the new datacube is identical to that used in the narrowband STAP [2, 4-6], and thus the 2D spreading of the clutter caused by the RM term is effectively eliminated.

Note that, like the classical 1D KT method, the transform in Eq. (53) also cannot eliminate the quadratic and higher order RM terms, but as mentioned before, the contributions of these terms are negligible for airborne array radar (small size) and short CPI. In practice, the proposed 2D transform in Eq. (53) can be also achieved by a 2D interpolation in the space-time domain for each range frequency [41]. Considering that there is actually no coupling between the slow-time and the along-array position in Eq. (52), the 2D transform can be decomposed into two 1D interpolations, i.e., the interpolations in the slow-time and spatial domains for each range frequency, which can reduce the computational burden.

We refer to the proposed algorithm as space-time keystone transform (ST-KT), and provide the signal processing flowchart in Fig. 9. In this algorithm, a FFT is first applied with respect to the fast-time (range) to transform the received datacube to the range frequency-space-time domain, followed by the two 1D interpolations to rescale the slow-time and along-array position, respectively. Afterwards, the data is transformed back into the fast-time domain via an inverse FFT (IFFT) with respect to the range frequency to generate the new datacube for the STAP operations. It is worth mentioning that, the order of the two 1D interpolations in the ST-KT can be exchanged, and we can either apply the interpolation in slow-time or along-array position first. In Fig. 10, a demonstration of the ST-KT (the two interpolations) to the 3D data are provided, where the proposed SK-KT looks like a 3D keystone in the range frequency-space-time domain.

Moreover, some of the computational efficient methods for classical KT, such as the chirp scaling based KT [42], and the chirp-Z based KT [43], can also be easily integrated into the

original datacube → **FFT in range** → **interpolation in slow-time** → **interpolation in along-array position** → **IFFT in range frequency** → new datacube

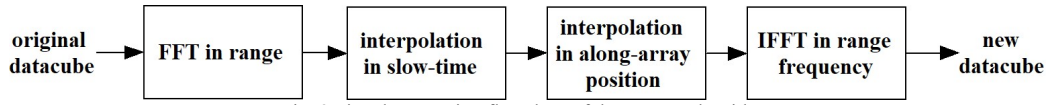Fig. 9 Signal processing flowchart of the ST-KT algorithm.

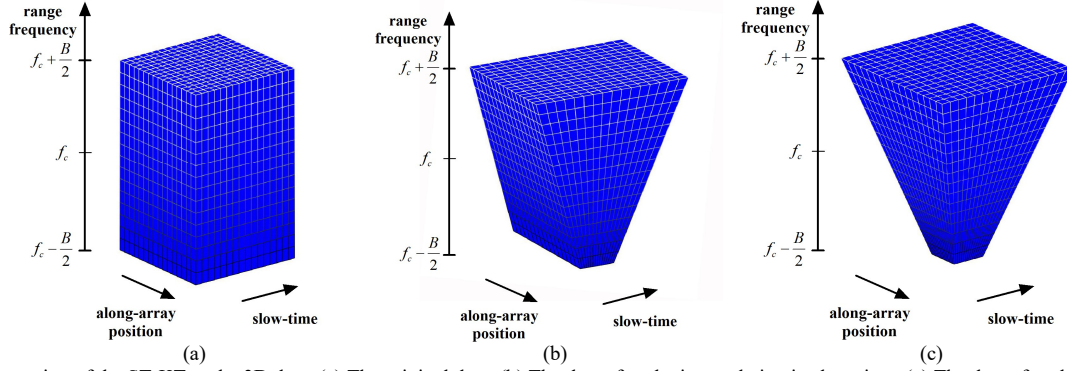(a)   (b)   (c)

Fig. 10 Demonstration of the ST-KT to the 3D data. (a) The original data. (b) The data after the interpolation in slow-time. (c) The data after the two interpolations.

proposed ST-KT algorithm, which can further improve the computational efficiency in practical exercises.

5.2 Simulation Results

In this subsection, simulated echo data of the ground clutter are generated to evaluate the capability of the proposed ST-KT algorithm to eliminate the 2D spectrum spreading. To simulate the echoes of the ground clutter more realistically, millions of discrete clutter sources with random backscattering coefficients are set on the ground, each of which generates an echo signal independently for an airborne array radar. The distance between each pair of the adjacent clutter sources is set to be less than either of the range and azimuth resolutions, and the amplitudes of the clutter sources are zero-mean complex Gaussian distributed random variables with identical variance and independent with each other. The echo signals from all the clutter sources are finally summed up and compressed in range to generate a 3D datacube, which is then used as samples to test the performance of the STAP algorithms. The major parameters for this simulation are listed in Table II.

TABLE II
PARAMETERS FOR THE GROUND CLUTTER DATA SIMULATION

Parameter	Value
Carrier frequency	1GHz
Bandwidth	240MHz
Platform speed	75m/s
Crab angle	20°
PRF	1000Hz
Number of array elements	32
Number of coherent processing pulses	32
Inter-element distance of the ULA	Half-wavelength
Elevation of the scene center	30°
Antenna pattern	Cosine type without backlobe
Number of clutter sources on the ground	4000(range)* 5000(azimuth)
Distance between the scene center and radar	15km
Input clutter-to-noise ratio per element per pulse	20dB

Fig. 11 illustrates the feasibility of the proposed ST-KT algorithm by the estimated MVDR spectra when KTs is applied on the datacube or not. All the spectra are estimated from the simulated datacube using 512 range samples. In Fig. 11 (a), as we can see, the MVDR spectrum spreads obviously in the 2D frequency domain, like that shown in Fig. 6 (a). To compare the performance of the proposed 2D ST-KT to that of the traditional 1D KT algorithm, we first apply slow-time domain KT and spatial domain KT respectively to the datacube, and show the corresponding MVDR spectra in Fig. 11 (b) and (c). As we can see, neither of the 1D KTs can fully solve the spectrum spreading problem, although they have the ability to eliminate part of the spreading. Take Fig. 11 (c) for example, applying a spatial (cross-array) KT can only eliminate the spectrum spreading in the area where the Doppler frequency is close to 0. In Fig. 11 (d), the MVDR spectrum is estimated after applying ST-KT to the datacube. As we can see, the spreading of the clutter in the 2D frequency domain is totally eliminated, similar to the MVDR spectrum in case of narrowband.

Figs. 12 and 13 evaluate the performance of the proposed ST-KT algorithm by the estimated SCNR loss when the ST-KT is applied on the datacube or not. All the curves are calculated via Eq. (51), with $\mathbf{R}$ replaced by the estimated covariance matrix. To provide a deep investigation on the improvements brought by ST-KT, we first assume that the bandwidth just affects the echo of the ground clutter, but has no influence on the moving target signals. That means the target steering vector in Eq. (51), i.e., $\mathbf{v}(f_d, f_s)$, is assumed to be single-frequency in the space-time domain, as that used in the traditional narrowband STAP, when calculating the SCNR loss curves. The related results are shown in Fig. 12. As we can see, ST-KT narrows the clutter suppressing notches for both the fully STAP and JDL STAP algorithms, implying improved slow-moving target detection performance in case of wideband. Moreover, by comparing the two subfigures, we find the improvement brought by ST-KT in terms of the width of the clutter suppressing notch is more evident for the reduce-dimension STAP method. This behavior is really desirable, since in most practical applications, reduce-dimension STAP methods are used instead of fully STAP methods due to computational efficiency as well as fast convergence.

Note that, although the SCNR loss curves shown in Fig. 12 have indicated the improvement brought by ST-KT, there is still a key factor not considered when generating the curves. That is
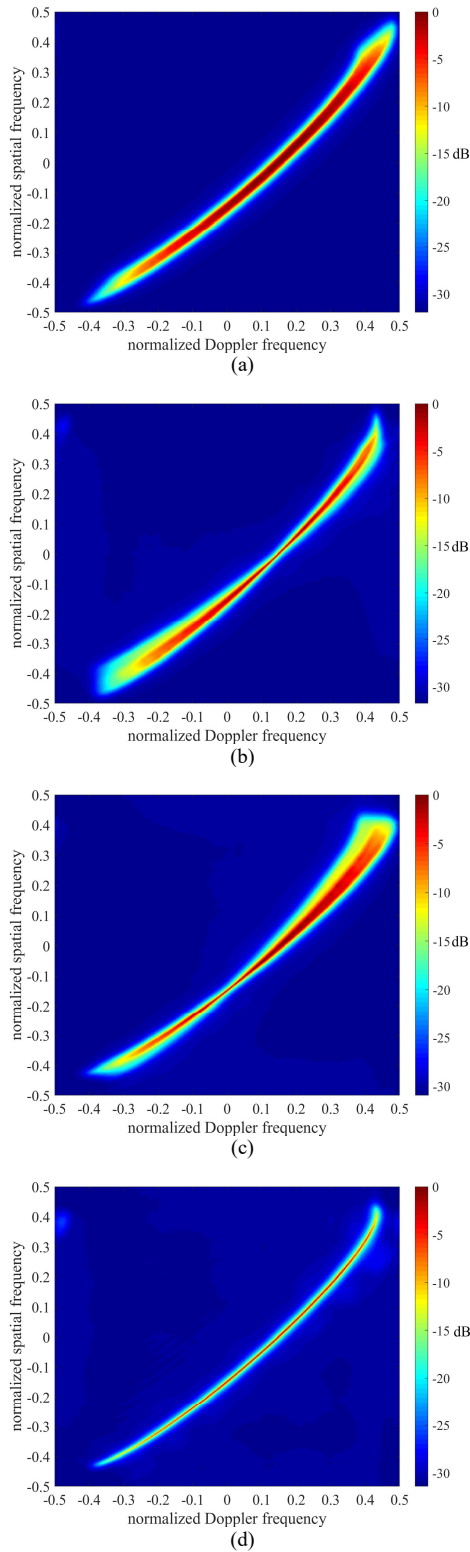

Fig. 11 Estimated MVDR spectra of the simulated ground clutter with and without KTs. (a) Spectrum is generated without KT. (b) Spectrum is generated with slow-time domain KT. (c) Spectrum is generated with spatial domain KT. (d) Spectrum is generated with 2D ST-KT.

the influence of bandwidth on the echoes of the moving targets. When the bandwidth increases, the RM within the snapshot induced by platform motion as well as self-motion for moving target is not negligible, and should also be considered when evaluating the performance of the STAP methods. Therefore, we now consider that the bandwidth affects both the echo signals of the ground clutter and moving targets. The target steering vector is generated via the signal model proposed in Section II when calculating the SCNR loss curves, and the results are shown in Fig. 13. As we can see, without ST-KT, the performance of the fully STAP and JDL STAP methods in terms of the SCNR is even poorer, as compared to Fig. 12. The output SCNR drops significantly not only for slow-moving targets but also for fast-moving targets. This is because in the traditional STAP algorithms, the target steering vector used to generate the adaptive weight differs from the real target steering vector in case of wideband. This mismatch will then attenuate the power of moving target when it passes the so-called matched filter in the architecture of the STAP filter. With the relative velocity between the platform and the moving target increasing, the RM within the snapshot becomes more evident, leading to the increasing mismatch between the two steering vectors.

It also can be seen from the two figures that, the curves estimated from the datacube with ST-KT change slightly as compared to the counterparts shown in Fig. 12. To explain that,
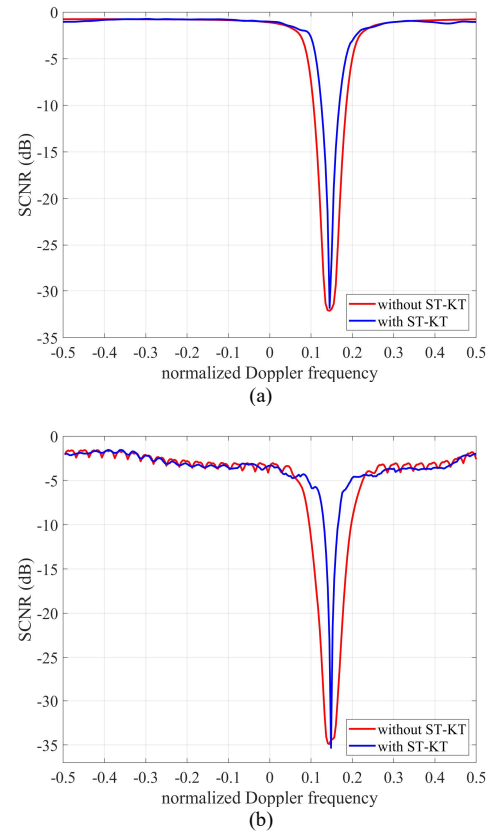

Fig. 12 Estimated SCNR loss curves with and without ST-KT when the influence of bandwidth on the moving target signal is not considered. (a) SCNR loss curves for fully STAP. (b) SCNR loss curves for 3×3 JDL STAP algorithm.
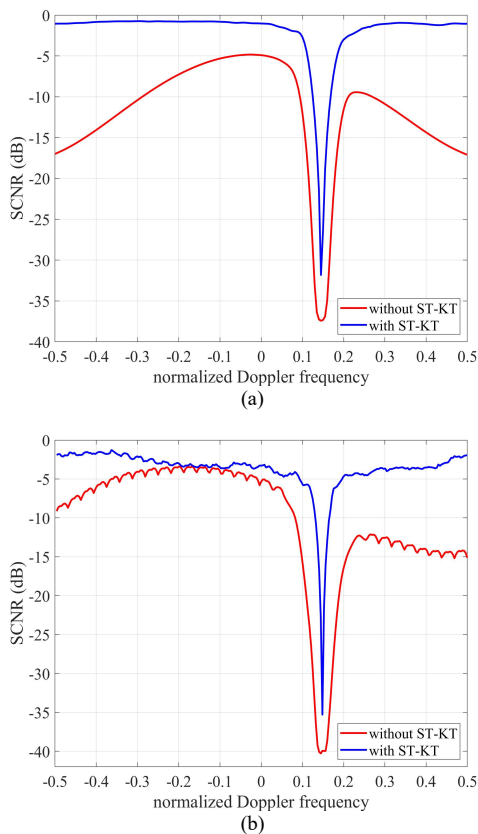
Fig. 13 Estimated SCNR loss curves with and without ST-KT when the influence of bandwidth on the moving target signal is considered. (a) SCNR loss curves for fully STAP. (b) SCNR loss curves for 3×3 JDL STAP algorithm.

we first remember that the traditional 1D KT is originally designed for moving target imaging. It has the ability to compensate arbitrary linear RM of the target to be imaged, including that induced by platform motion, self-motion, or both of them. When it is extended to the space-time domain, this desirable ability remains. Therefore, after ST-KT, the moving target is 'refocused' and the mismatch between the target steering vector used to generate the adaptive weight and the real steering vector is eliminated.

By comparing the SCNR curves in Fig. 13, it is seen that the proposed ST-KT algorithm significantly improves the performance of W-STAP, in terms of the output SCNR for both slow-moving and fast-moving targets.

After the testing of the SCNR curves, we now use the simulated moving targets to compare different STAP methods in case of wideband (the radar bandwidth is set to be 240MHz). Two simulated moving targets, referred to as target 1 and target 2, are added in the simulated clutter plus noise background. Both of the two targets are localized at the boresight direction of the beam (with normalized spatial frequency equal to 0). Target 1 is used to denote a slow-moving target (with self-motion induced normalized Doppler display equal to 0.06), and target 2 is used to simulate a fast-moving target (with self-motion induced normalized Doppler display equal to 0.28). The input SNR (per element per pulse) of the two targets are set to be 5dB and 0dB, respectively. In Fig. 14 (a), the range-Doppler

(RD) map of the simulated data (including targets, clutter, and noise) is shown, where the positions of the two targets are marked by the red squares. In Fig. 14 (b), the RD map of the simulated data with respect to the two moving targets (where the clutter and noise is absent) is shown.

To test the ability of ST-KT to refocus moving targets, the RD maps of the two moving targets before and after ST-KT processing are provided in Figs. 15 and 16 (contour figures are employed to demonstrate the changes more clearly). It is clearly seen from these figures, the ST-KT refocuses both of the two moving targets, and thereby reduces the SCNR loss caused by motion-induced defocusing. Moreover, by comparing Figs. 15 and 16, we find that the improvement of SCNR for the fast-moving targets is more significant than that for the slow-moving targets (which can be also seen in Fig. 13). This is because that the defocusing induced by self-motion of fast-moving targets is even worse than that of the slow-moving target, and ST-KT can refocus moving targets with arbitrary linear range mitigations. Hence, the enhancement of signal power brought by ST-KT is more significant for the fast-moving targets.

Now, the improvement of the moving target detection ability brought by ST-KT for W-STAP is verified by the output residue (output power after adaptive processing) with respect to the two moving targets. Three STAP approaches i.e., the traditional JDL algorithm, the JDL algorithm with sub-band processing, and the JDL algorithm with ST-KT, are utilized to process the
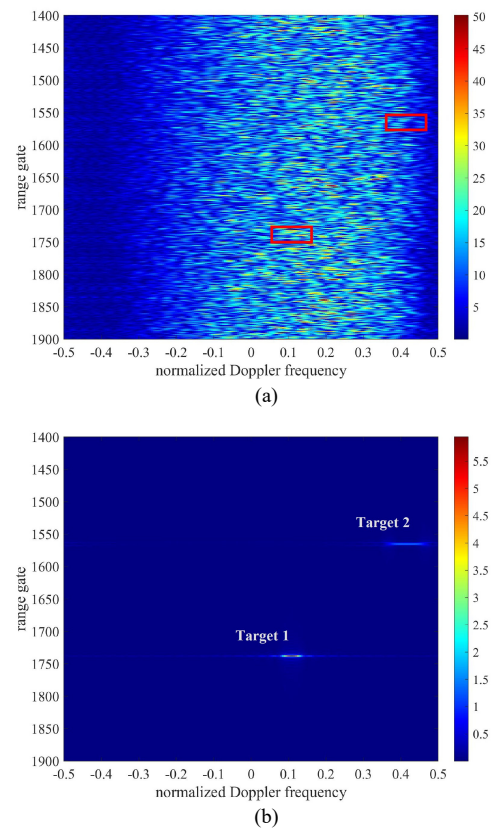

Fig. 14 Range-Doppler maps of the simulated data. (a) RD map of the entire simulated data (including moving targets, clutter, and noise). (b) RD map of the interference-free data.

simulated data separately for comparison. The number of the training samples for all the three methods is set to be 40, and the number of sub-band is set to be 8 (the bandwidth of each sub-band is 30MHz) when applying the sub-band STAP
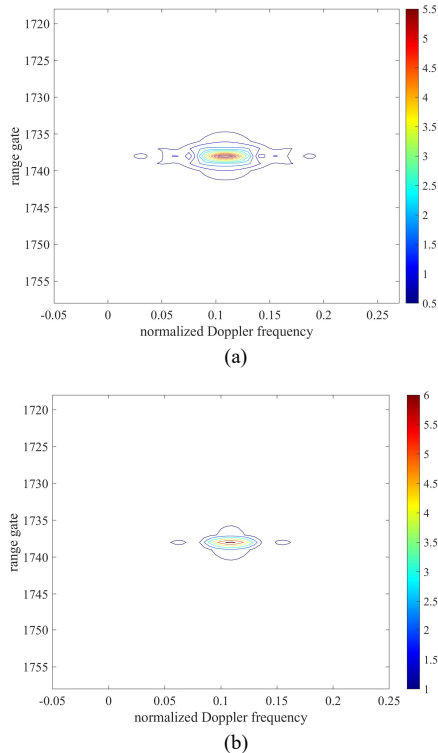

(a)

(b)

Fig. 15 Range-Doppler maps of Target 1 before and after ST-KT. (a) RD map before ST-KT. (b) RD map after ST-KT.
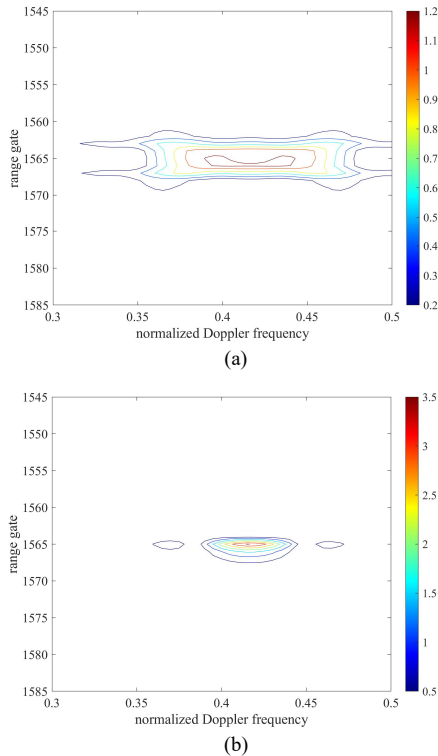

(a)

(b)

Fig. 16 Range-Doppler maps of Target 2 before and after ST-KT. (a) RD map before ST-KT. (b) RD map after ST-KT.

approach. Fig. 17 shows the range profiles of the output residue for the Doppler bins where the two moving targets are present. In both of the two subfigures, the moving targets are localized in the center. As we can see, both the sub-band processing method and ST-KT based STAP method overperform the traditional STAP method in terms of the output SCNR for moving targets. However, the improvement brought by sub-band processing is limited, as it cannot eliminate the 2D spectrum spreading thoroughly. Among all the three approaches, the ST-KT method gains the best performance in terms of the output SCNR for both the fast-moving and slow-moving moving targets.

Considering that STAP is designed not only to mitigate the ground clutter but also to suppress the jamming, we now add a jamming source into the simulation and evaluate the performance of the proposed ST-KT in the environment where both clutter and jamming are present. A land-based barrage noise jamming is considered here as an example. Both the azimuth and elevation angles of the jamming source are set to be 30°, and the jamming-to-noise ratio (JNR) is 35dB. Then, the echo signals from the simulated ground clutter as well as this jamming are summed up and compressed in range to generate the datacube.

In Fig. 18, the estimated MVDR spectra from the datacube with and without KTs are provided to validate the ST-KT algorithm in the clutter-plus-jamming environments. As mentioned in the literature [2-6], jamming is assumed to be uncorrelated between pulses but correlated between array elements. That is to say, the contribution of jamming in the
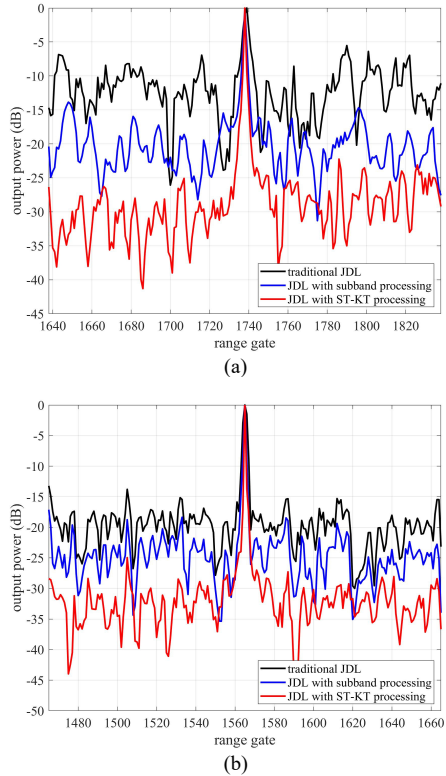

(a)

(b)

Fig. 17 Range profiles of the output residue with respect to the two moving targets. (a) Range profile of the output residue for Target 1. (b) Range profile of the output residue for Target 2.

temporal domain is identical to that of noise, while the contribution in the spatial domain is the same as that of the point-target. Thus, in case of narrowband, the echo of jamming is recognized as the signal-frequency signal in the spatial

Fig. 18 Estimated MVDR spectra of the simulated ground clutter and jamming with and without KTs. (a) Spectrum is generated without KT. (b) Spectrum is generated with slow-time domain KT. (c) Spectrum is generated with spatial domain KT. (d) Spectrum is generated with 2D ST-KT.

domain, but occupies all the Doppler band. However, with increasing bandwidth, dispersion of jamming is deteriorated across the array, leading to the spectrum spreading in the spatial frequency domain, which is clearly shown in Fig. 18 (a). Since the spreading is in the spatial frequency domain, the traditional time-domain KT fails to eliminate it, as shown in Fig. 18 (b). The spreading spectrum of jamming causes a broadened jamming suppression notch, thereby degrades the performance of the traditional STAP methods. From our discussion made in Section III, it can be deduced that the dispersion of jamming in the spatial domain is induced by the RM in the spatial domain, referred to as aperture fill in the field of array processing. Hence, it is expected to address this problem via spatial domain KT. In Fig. 18 (c), the estimated spectrum from the datacube with 1D spatial domain KT is shown. As we can see, as compared to Fig. 18 (a), the spreading of jamming in the spatial frequency is well eliminated, although the spreading of clutter is not totally solved, which is the same as that shown in Fig. 11 (c). Fig. 18 (d) shows the MVDR spectrum estimated from the datacube when ST-KT is applied. Both the spectrum spreading with respect to the clutter and jamming are eliminated, demonstrating that our proposed algorithm is also promising in the environment where both clutter and jamming are present.

VI. CONCLUSION

With increasing bandwidths, the narrowband assumption employed in the traditional STAP theory becomes invalid, and the performance of the corresponding STAP methods drops significantly. This paper focuses on the clutter suppression for wideband radar STAP. A generalized echo signal model of the ground clutter for airborne pulse-Doppler radar with array antenna is established. Based on this model, analytical expressions have been derived to quantitatively describe the 2D spreading of the ground clutter. Moreover, the contribution of the ground clutter to space-time snapshots as well as the clutter covariance matrix is presented in the wideband cases, and the performance loss of the output SCNR is also analyzed in detail.

Finally, to remedy the degrading performance of the current STAP methods in wideband cases, a 2D ST-KT algorithm is proposed to eliminate the decorrelation within the snapshot. As validated by simulation results, after applying ST-KT to the datacube prior to adaptive processing, both traditional fully and partial STAP algorithms gain significant improvement in terms of the output SCNR for both slow-moving and fast-moving targets, as compared to the case when ST-KT is not applied, which proved the feasibility of this proposed algorithm for W-STAP.

REFERENCES

[1] W. L. Melvin and J. A. Scheer, 'Principles of Modern Radar, Vol. II: Advanced Techniques'. Edison, NJ: SciTech Publishing, 2013.

[2] Melvin W.L.: 'a STAP overview'. IEEE AES Syst. Mag., 2004, 19(1): 19~35.

[3] Brennan L.E., and Reed I.S.: 'Theory of adaptive radar'. IEEE Trans. Aerosp. Electron. Syst., 1973, 9 (2): 237~252.

[4] Ward J.: 'Space-Time Adaptive Processing for Airborne Radar'. Technical Report ESC 1015, MIT Lincoln Laboratory, Lexington, MA, 1994.
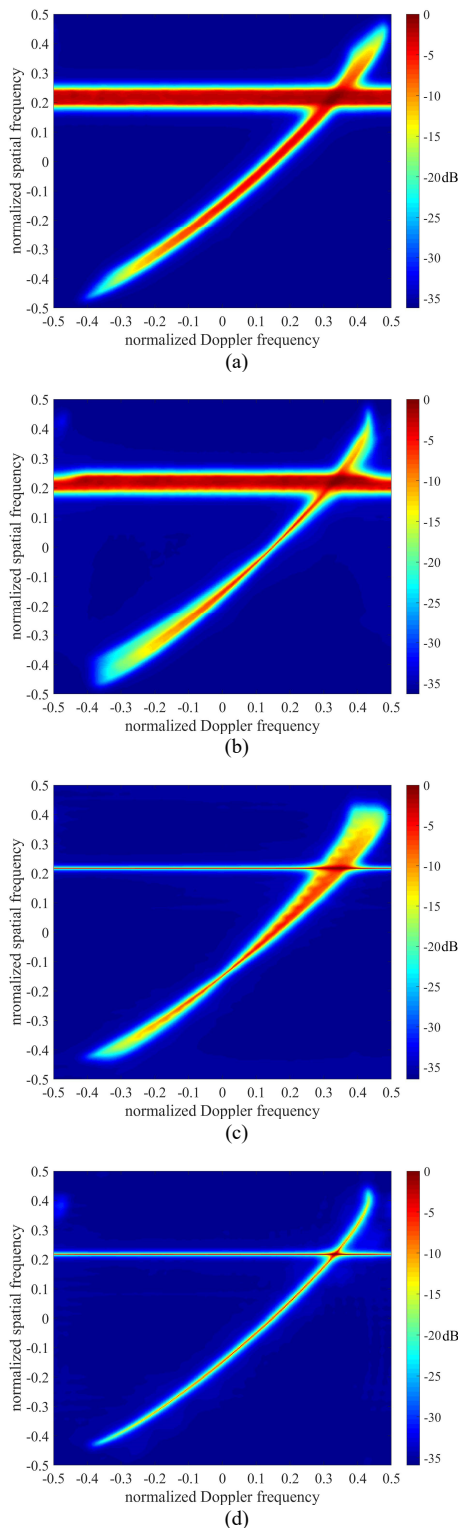
> REPLACE THIS LINE WITH YOUR PAPER IDENTIFICATION NUMBER (DOUBLE-CLICK HERE TO EDIT) <   17

[5]   J. Guerci, 'Space-Time Adaptive Processing for Radar, Second Edition'. Norwood, MA: Artech House, 2014.

[6]   R. Klemm, 'Principles of Space-Time Adaptive Processing, 3rd Edition'. IET, London, UK, 2006.

[7]   I. S. Reed, J. D. Mallett, L. E. Brennan. 'Rapid convergence rate in adaptive arrays'. IEEE Trans. Aerosp. Electron. Syst., 1974, 10(6): 853~863.

[8]   R. Klemm. 'Adaptive airborne MTI: an auxiliary channel approach. Communications'. Radar and Signal Processing, IEE Proceedings F, 1987, 134(3): 269~276.

[9]   Wang H , Cai L . 'On adaptive spatial-temporal processing for airborne surveillance radar systems'. IEEE Trans. Aerosp. Electron. Syst., 1994, 30(3): 660-670.

[10] A. Haimovich, M. Berin. 'Eigenanalysis-based space-time adaptive radar: performance analysis'. IEEE Trans. Aerosp. Electron. Syst., 1997, 33(4): 1170~1179.

[11] J. S. Goldstein, I. S. Reed, P. A. Zulch. 'Multistage partially adaptive STAP CFAR detection algorithm'. IEEE Trans. Aerosp. Electron. Syst., 1999, 35(2): 645~661.

[12] M Steiner, K Gerlach. 'Fast Converging Adaptive Processor or a Structured Covariance Matrix'. IEEE Trans. Aerosp. Electron. Syst., 2000, 36(4): 1115~1126.

[13] W Titi, D. F. Marshall. 'The Arpa/Navy Mountaintop program: adaptive signal processing for airborne early warning radar'. Proc. of IEEE ICASSP, 1996: 1165~1168.

[14] M. O. Little, W. P. Berry. 'Real-time multichannel airborne radar measurements'. Proc. of the IEEE National Radar Conf., Syracuse, NY, USA, 1997: 138~142.

[15] W. L. Melvin. 'Space-time Adaptive Radar Performance in Heterogeneous Clutter'. IEEE Trans. Aerosp. Electron. Syst., 2000, 36(2): 621~633.

[16] A. K. Shackelford, K. Gerlach, S. D. Blunt. 'Partially adaptive STAP using the FRACTA algorithm'. IEEE Trans. Aerosp. Electron. Syst., 2009, 45(1): 58-69.

[17] K. Gerlach, M. L. Picciolo. 'Robust STAP using reiterative censoring'. Proc. of the IEEE Radar Conf., Huntsville, Alabama, USA, 2003: 244~251.

[18] A. Barros Cardoso da Silva, S. Baumgartner and G. Krieger, 'Training Data Selection and Update Strategies for Airborne Post-Doppler STAP'. IEEE Trans. Geosci. Remote Sens., 2019, 57(8): 5626-5641.

[19] J. R. Guerci. 'Knowledge-Aided Adaptive Radar at DARPA: An Overview'. IEEE Signal Processing Magazine, 2006, 23(1): 41~50.

[20] J. Cuerci. 'Cognitive Radar: The Knowledge-Aided Fully Adaptive Approach'. Norwood, MA: Artech House, 2010.

[21] A. De Maio, A. Farina, G. Foglia. 'Knowledge-Aided Bayesian Radar Detectors & Their Application to Live Data'. IEEE Trans. Aerosp. Electron. Syst., 2010, 46(1): 170~183.

[22] G. Sun, Z. He, J. Tong and X. Zhang, "Knowledge-Aided Covariance Matrix Estimation via Kronecker Product Expansions for Airborne STAP," IEEE Geosci. Remote Sens. Lett., 2018, 15(4): 527-531.

[23] G. Sun, M. Li, J. Tong and Y. Ji, 'Structured Clutter Covariance Matrix Estimation for Airborne MIMO Radar With Limited Training Data'. IEEE Geosci. Remote Sens. Lett., Early Access, doi: 10.1109/LGRS.2020.3027818.

[24] J. Mayhan, A. Simmons and W. Cummings, 'Wide-band adaptive antenna nulling using tapped delay lines'. IEEE Transactions on Antennas and Propagation, 29(6), pp. 923-936, 1981.

[25] W. Liu and S. Weiss, 'Wideband Beamforming: Concepts and Techniques'. Chichester, U.K.: Wiley, 2010.

[26] X. Yang, S. Li, Y. Sun, T. Long and T. K. Sarkar, 'Robust Wideband Adaptive Beamforming With Null Broadening and Constant Beamwidth'. IEEE Transactions on Antennas and Propagation, 2019, 67(8): 5380~5389.

[27] Y. Bucris, I. Cohen, and M. A. Doron, 'Bayesian focusing for coherent wideband beamforming', IEEE Trans. Audio, Speech, Language Process., 2012, 20(4): 1282~1296.

[28] R. Ebrahimi and S. R. Seydnejad, 'Elimination of pre-steering delays in space-time broadband beamforming using frequency domain constraints'. IEEE Commun. Lett., 2013, 17(4): 769~772.

[29] W. Liu, S. Weiss, J. G. McWhirter, and I. K. Proudler, 'Frequency invariant beamforming for two-dimensional and three-dimensional arrays'. Signal Process., 2009, 87(11): 2535~2543.

[30] M. Zatman, 'How narrow is Narrowband?'. IEE Proceedings: Radar, Sonar, and Navigation, 1998, 145(2): 85~91.

[31] G. M. Herbert, 'Space-time adaptive processing (STAP) for wide-band airborne radar'. IEEE 2000 International Radar Conference, Alexandria, VA, USA, 2000: 620~625.

[32] A. O. Steinhardt and N. B. Pulsone, 'Subband STAP processing, the fifth generation'. Proceedings of the 2000 IEEE Sensor Array and Multichannel Signal Processing Workshop. Cambridge, MA, USA, 2000: 1~6.

[33] H. Mir and Z. Berkowitz, 'Sub-band STAP for stretch processed systems'. 2009 IEEE International Conference on Acoustics, Speech and Signal Processing, Taipei, 2009: 2025~2028.

[34] A. Hoffman and S. M. Kogon, 'Subband STAP in wideband radar systems'. Proceedings of the 2000 IEEE Sensor Array and Multichannel Signal Processing Workshop, Cambridge, MA, USA, 2000: 256~260.

[35] S. U. Pillai, K. Y. Li and J. R. Guerci, 'Effect of Bandwidth on Wideband-STAP Performance'. 2007 Conference Record of the Forty-First Asilomar Conference on Signals, Systems and Computers, Pacific Grove, CA, 2007: 2195~2198.

[36] S. U. Pillai, J. R. Guerci and S. R. Pillai, 'Wideband STAP (WB-STAP) for passive sonar'. Oceans 2003. Celebrating the Past ... Teaming Toward the Future, San Diego, CA, USA, 2003, Vol.5: 2814~2818.

[37] K. Y. Li, U. S. Pillai, P. Zulch and M. Callahan, 'A Modulation Based Approach to Wideband-STAP'. 2007 Conference Record of the Forty-First Asilomar Conference on Signals, Systems and Computers, Pacific Grove, CA, 2007: 1825~1829.

[38] C. Zhu, D. Wu and M. Shen, 'A Two-dimensional Keystone Transformation Algorithm for Wideband Space-Time Adaptive Processing'. 2019 6th Asia-Pacific Conference on Synthetic Aperture Radar (APSAR), Xiamen, China, 2019: 1~4.

[39] Gradshteyn I.S., Rhyzhik I.M.: 'Table of Integrals, Series, and Products, 8th Edition'. Academic Press, San Diego, 2014.

[40] R. Lanari and G. Fornaro, 'A short discussion on the exact compensation of the SAR range-dependent range cell migration effect'. IEEE Trans. Geosci. Remote Sens. 1997, 35(6): 1446-1452.

[41] R. P. Perry, R. C. Dipietro, and R. L. Fante, 'SAR imaging of moving targets'. IEEE Trans. Aerosp. Electron. Syst., 1999, 35(1): 188~200.

[42] D. Zhu, Y. Li and Z. Zhu, 'A Keystone Transform Without Interpolation for SAR Ground Moving-Target Imaging'. IEEE Geosci. Remote Sens. Lett., 4(1): 18~22.

[43] O. Çulha and Y. Tanik, 'Low Complexity Keystone Transform and Radon Fourier Transform Utilizing Chirp-Z Transform'. IEEE Access, 2020, vol. 8: 105535~105541.